Multiple-beam X-ray interferometry for phase-contrast microtomography

Ulrich Bonse[a]* and Felix Beckmann[b]

[a]*Institute of Physics, University of Dortmund, D-44221 Dortmund, Germany, and* [b]*Hamburger Synchrotronstrahlungslabor (HASYLAB) at Deutsches Elektronen-Synchrotron (DESY), Notkestrasse 85, D-22603 Hamburg, Germany. E-mail: bonse@physik.uni-dortmund.de*

The first successful operation of an X-ray interferometer under conditions of non-planar three-beam diffraction for phase-contrast X-ray microtomography is reported. Intrinsic phase differences of the reflections used cancel from the three-dimensional phase image of the specimen. With simultaneous hkl and $hk\bar{l}$ reflections of a synchrotron radiation beam in a side-by-side geometry, the size of the usable field of view is doubled and the investigated specimen volume is increased by a factor of four. As an example, the reconstructed slice of a mouse kidney is shown in phase contrast at 71 keV. Optimized choices of three-beam reflections and matching interferometer geometries useful for applications are presented.

Keywords: microtomography; multiple-beam X-ray interferometry; phase-contrast microtomography.

1. Introduction

In recent years, with the increasing use of synchrotron radiation, microtomography (μCT) has become a powerful tool for performing three-dimensional studies of structures on the mesoscopic scale with spatial resolutions ranging from 0.5 μm to 20 μm. Results have been summarized, for instance, in reviews by Graeff & Engelke (1991), Kinney & Nichols (1992), Graeff (1996) and Bonse & Busch (1996). In most cases it has been sufficient to simply employ X-ray attenuation for achieving the necessary image contrast. However, attenuation contrast is very poor with specimens consisting predominantly of light elements like biological tissues or resin-based materials. To reveal structures in light specimens, X-ray phase-contrast microtomography (PμCT), generated by placing the specimen in one of the interfering beams of an X-ray interferometer (Bonse & Hart, 1965*a*), is an excellent alternative (Momose *et al.*, 1995; Beckmann *et al.*, 1995, 1997) to attenuation contrast.

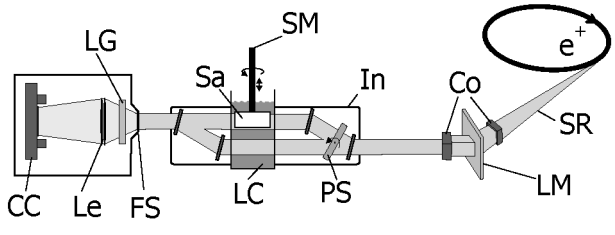

Figure 1
Phase-contrast microtomography (PμCT) using ≥70 keV synchrotron radiation. e^+: synchrotron radiation source; LM: Laue monochromator; Co: collimators; In: interferometer manufactured of a perfect silicon crystal; Sa: sample; SM: sample manipulator; LC: liquid cell; PS: phase shifter; FS fluorescent screen; CC: CCD detector; Le: lens imaging FS to CC; LG: lead glass.

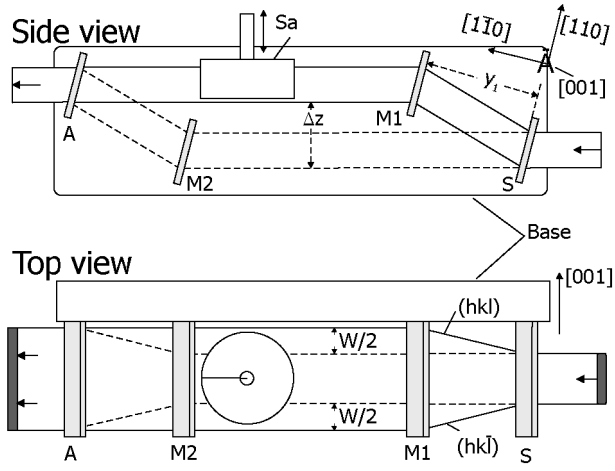

Figure 2
X-ray interferometer using simultaneous three-beam case diffraction hkl, $hk\bar{l}$. S, M1, M2, A: Bragg diffracting crystal wafers for coherent splitting and superposition of interfering beams. Sa: sample; $\Delta z(W)$: separation of beams in vertical (horizontal) direction. Note doubling of incident beam width X_0 when $W = X_0$.

State-of-the-art PμCT using synchrotron radiation is based on generating parallel projections of the cylindrical specimen by employing a low-divergence synchrotron radiation beam of sufficient width X_0 to illuminate the entire diameter of the specimen. Since there are increasing requests to study specimens with diameters exceeding the beam width of most synchrotron radiation sources, some means of beam widening are required. It is the purpose of this investigation to demonstrate that, by establishing three-beam diffraction in the phase-sensing interferometer, widths X_0 given by the synchrotron radiation source can be doubled. The principle of this method and its actual use in an experiment performed at the synchrotron radiation source DORIS at DESY, Hamburg, will be described.

2. Principle of multiple-beam interferometry

The general set-up of the PμCT camera is shown in Fig. 1. Synchrotron radiation with energies E in the range 60–200 keV generated by wiggler BW5 is made monochromatic to a relative bandwidth of $\Delta E/E \simeq 10^{-3}$ by Bragg reflection in transmission (Laue) geometry from a single-crystal monochromator LM. Fig. 2 shows, in a side and a top view, the skew-symmetric X-ray interferometer (Bonse & Hart, 1965*b*) featuring a long section of parallel interfering beams between mirrors M1 and M2. Transmitted beams at mirrors M1 and M2 have been omitted in the drawing. The upper beam (Fig. 2, side view) propagates through the sample, Sa, which normally is a cylinder with axis vertical and located inside a fluid-containing measuring cell, LC (Fig. 1). Wafers M2 and A serve to recombine both beams to form the interference pattern

which carries phase-contrast encoded information about the structure of Sa. The pattern is recorded by an area detector consisting of the fluorescent screen FS (Fig. 1), the optical lens, Le, and the CCD detector, CC. The phase shifter, PS, is used to determine the projected phase shift modulo 2π. Details of the phase extraction and the elimination of the 2π ambiguity from the interference pattern have been described by Beckmann *et al.* (1997).

Equation (18) below gives the separation Δz of the interfering beams in the vertical plane (Fig. 2, side view). As may be seen, in order to accommodate at high energies a sufficient portion of a longer sample within only the upper beam, higher-order reflections have to be used and the distance y_1 (Fig. 2) must be increased. To give an example, with 70 keV X-rays a good choice of high-order reflection would be 660 with Bragg angle $\Theta_B = 7.953°$. Making $y_1 = 27.8$ mm, sufficient vertical beam separation of 7.69 mm is achieved.

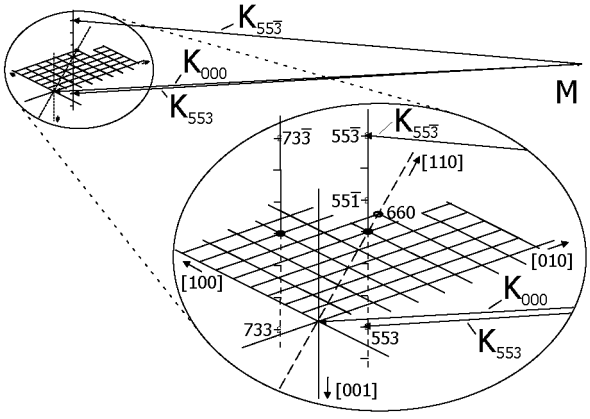

Figure 3
Three-beam diffraction hkl, $hk\bar{l}$ explained in reciprocal space. M: center of Ewald sphere. For 553, 553̄ the waves are shown. Further possible cases, *e.g.* 551, 551̄ and 733, 733̄, are indicated.

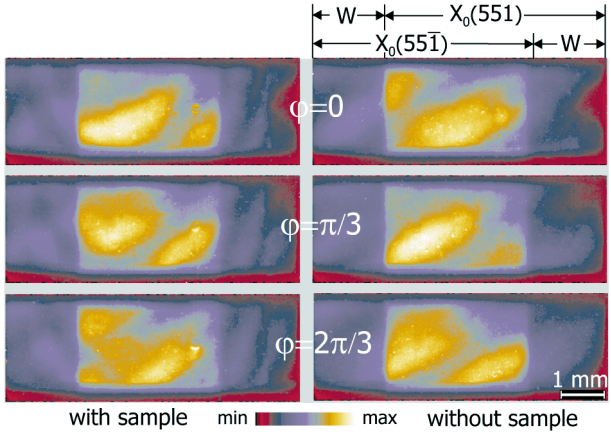

Figure 4
Set of projections taken at fixed angular sample position and at three different values of overall phase shift φ, with and without the specimen (mouse kidney) in the beam. $E = 71$ keV. X_0: width of incident beam. The incomplete horizontal separation W of beams ($W < X_0$) did not hamper the tomographic reconstruction (in this pilot experiment) (Fig. 5).

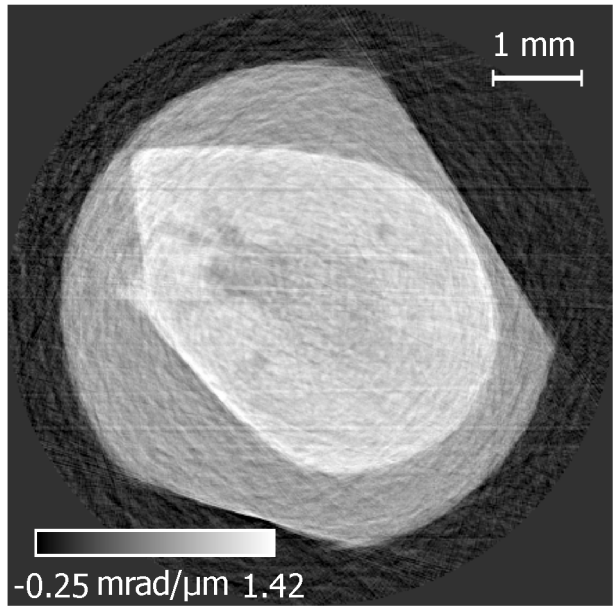

Figure 5
One reconstructed 16.2 μm-thick slice of mouse kidney specimen. Center bright structure: tissue. Note phase shift modulations. Grey ring: embedding epoxy; black area: water (cell fluid). Bar: phase advance of wave per μm path relative to water. The phase advance is approximately proportional to mass density. From this the spatial mass density distribution of this slice of kidney is found to range between 1.182 g cm^{-3} and 1.224 g cm^{-3}. $E = 71$ keV.

Three-beam diffraction by a wavevector triplet of type $\{\mathbf{K}_{hkl}, \mathbf{K}_{hk\bar{l}}, \mathbf{K}_{000}\}$ can be employed for widening the field of view in the horizontal direction. For the upper (lower) beam in Fig. 2 the widening occurs through reflection by wafer S (M_2). In order to avoid at M1 and A the direct generation of (hkl) beams by ($hk\bar{l}$) beams (and *vice versa*), we exclude even values of h, k, l which guarantees the difference reflection (0 0 2l) to be forbidden in the diamond lattice. The geometrical situation in reciprocal space is illustrated in Fig. 3. The horizontal plane in real space is given by the incident wave $\mathbf{K}_{000}$ together with the diffractometer axis [001], and a vertical plane is indicated as a rectangular net. $\mathbf{K}_{000}$ is orthogonal to [001] and has been drawn from the center of the Ewald sphere, M, to the origin of the reciprocal lattice. Some reflection pairs of $h\ k \pm l$ type, *i.e.* {551, 551̄}, {553, 553̄} and {733, 733̄} are shown. Starting from the 660 point, only small changes of direction and/or energy of the incident $\mathbf{K}_{000}$ will be sufficient to excite a three-beam diffraction with one or the other of the pairs. As an example, the wave vectors of the three-beam diffraction $\{\mathbf{K}_{553}, \mathbf{K}_{55\bar{3}}, \mathbf{K}_{000}\}$ are explicitly drawn in Fig. 3. Beams reflected as pairs separate from each other in the (horizontal) [001] direction (Fig. 2, top view). Equation (19) below gives the separation W acquired when the beam hits the next crystal wafer.

3. Pilot experiment

To demonstrate the feasibility of three-beam diffraction in PμCT, we investigated a mouse kidney specimen in a pilot

experiment using the X-ray interferometer shown in Fig. 2 working with the $\{\mathbf{K}_{551}, \mathbf{K}_{55\bar{1}}, \mathbf{K}_{000}\}$ triplet and an X-ray energy of 71 keV. We made y_1 = 27.8 mm, the distance between M1 and M2 be 34.5 mm, and the thickness of crystals S, M1, M2 and A be 0.7 mm. All wafers were 15 mm high and about 10 mm wide.

Fig. 4 shows projections with the kidney specimen inserted in the beam (left-hand side) and three projections without the specimen (right-hand side). Water was used as the cell fluid. Overall phase shifts are $\varphi = 0$, $\pi/3$ and $2\pi/3$. The phase shift induced by the sample is obtained by evaluating the change between projections on the left-hand side and projections on the right-hand side. Input data for tomographic reconstruction were collected by repeating the same set of exposures at 1° incremental rotations of the sample for a total of 180 angular positions. For reconstruction we used the method of filtered back-projections (Kak & Slaney, 1987). Fig. 5 shows one 16.2 µm-thick slice of the reconstructed specimen cylinder which was 2.0 mm in height. The kidney tissue is the bright structure in the center. Phase-shift modulations inside the specimen are recognizable. The tissue is surrounded by the embedding epoxy (grey). The black area is the cell fluid water. The bar at the bottom left indicates in a quantitative way the phase advance which the X-ray wave gains per µm path length travelled, relative to that when travelling in water. Since phase shift per path length is proportional to electron density and the latter is approximately proportional to mass density, we can re-calibrate the phase-shift scale directly to densities if we input the density value 1.18 g cm^{-3} of epoxy. From this we find the kidney density to range from 1.182 g cm^{-3} to 1.224 g cm^{-3}, which is reasonable.

On one of the projections in Fig. 4, the widths $X_0(551)$, $X_0(55\bar{1})$ and locations of the pictures due to the outgoing waves $\mathbf{K}_{551}$, $\mathbf{K}_{55\bar{1}}$ are indicated. Obviously both beams overlap in the center since their relative sidewise shift $W < X_0$. To make optimum use of the widening effect one should make $W = X_0$ and thereby double the beam width. This is straightforward by choosing y_1 larger and/or use a reflection with a larger l value. From the general calculations given in the final section we find that, by employing 553 reflections instead of the used 551, a field width of 10 mm would be obtained. For a particular synchrotron radiation beamline, the value of X_0 usually has to stay within narrow bounds. At BW5, X_0 is 5–6 mm so that a usable beam of width 10–12 mm can be obtained for PµCT by employing three-beam diffraction. It should be noted, however, that the reconstruction was not hampered by the partial overlap of beams in this pilot experiment.

4. Optimizing the choice of reflections and geometry

In order to survey the favorable choices of geometry and reflections for three-beam PµCT, we include a brief derivation of the underlying formalism. To be specific, we consider the three-beam reflection $\{\mathbf{K}_{hkl}, \mathbf{K}_{hk\bar{l}}, \mathbf{K}_{000}\}$ on the skew-symmetric interferometer shown in Fig. 2, but with a slightly more general choice of orientation. Our aim is to calculate the vertical distance Δz between interfering beams and the horizontal widening W of beams for a variety of reflections and crystallographic orientations of the interferometer and for different energies. In Fig. 2 we see that the unit normal $\mathbf{n}_c$ on the surfaces of the interferometer wafer crystals is defined by postulating that it has to be normal to the 'main' reflection $\mathbf{g}_{\rm main} = (h, k, 0)/a_0$ (generating the lower and upper interfering beams) and to the pair of 'sidewise splitting' reflections $\pm\mathbf{g}_{\rm split} = (0, 0, \pm l)/a_0$. Referring to crystallographic coordinates, this means that

$$\mathbf{n}_c = (k, \bar{h}, 0)/C^{1/2}, \tag{1}$$

with

$$C = h^2 + k^2. \tag{2}$$

Again from Fig. 2, we see that the unit normal $\mathbf{n}_b$ parallel to the interferometer's wafers and base is

$$\mathbf{n}_b = (h, k, 0)/C^{1/2}. \tag{3}$$

The diffraction vectors are

$$\mathbf{g}^+ = (h, k, l)/a_0, \qquad \mathbf{g}^- = (h, k, \bar{l})/a_0, \tag{4}$$

where a_0 = 0.543102 nm is the lattice parameter of silicon. The incident wave $\mathbf{K}_{000} = (K_1, K_2, K_3)$ has to be symmetric to the splitting reflections $\pm\mathbf{g}_{\rm split}$ given above which means that $K_3 = 0$. Diffracted waves are determined by Laue equations

$$\mathbf{K}_{hkl} = \left(K_1^+, K_2^+, K_3^+\right) = \mathbf{K}_{000} + \mathbf{g}^+, \tag{5}$$

$$\mathbf{K}_{hk\bar{l}} = (K_1^-, K_2^-, K_3^-) = \mathbf{K}_{000} + \mathbf{g}^-. \tag{6}$$

We combine equations (1)–(6) by elementary vector algebra under conditions of elastic scattering, *i.e.* $|\mathbf{K}_{hkl}| = |\mathbf{K}_{hk\bar{l}}| = |\mathbf{K}_{000}| = \lambda^{-1}$, where λ [nm] = 1.23985/E [keV] is the wavelength to be calculated from the used photon energy E. We arrive at equations quadratic in K_1, K_2, from which we obtain

$$K_1 = \lambda^{-1}\left[C^{-1}(kF\cos\Theta_{\rm B} - hG\sin\Theta_{\rm B})\right], \tag{7}$$

$$K_2 = \lambda^{-1}\left[C^{-1}(-hF\cos\Theta_{\rm B} - kG\sin\Theta_{\rm B})\right], \tag{8}$$

$$F = \left(C - l^2\tan^2\Theta_{\rm B}\right)^{1/2}, \tag{9}$$

$$G = \left(C + l^2\right)^{1/2}, \tag{10}$$

and $\Theta_{\rm B}$ is the Bragg angle. The condition for the quadratic equation to yield real-valued roots K_1 and K_2 is found to be

Table 1
Exemplary choices of three-beam reflections $h\ k\ \pm l$ yielding optimal vertical beam separation [Δz of equation (18)] and horizontal beam widening [W of equation (19)].

E: photon energy; λ: wavelength, θ_B: Bragg angle.

E (keV)	λ (nm)	hkl	θ_B (°)	Δz (mm)	W (mm)
80	0.0155	533	5.368	5.274	5.464
80	0.0155	553	6.292	6.396	5.743
80	0.0155	733	6.706	6.889	5.477
20	0.0620	131	10.91	10.03	6.489
20	0.0620	331	14.40	13.64	6.578
20	0.0620	511	17.25	16.18	6.672

$$\lambda \leq \lambda_{\max} = 2a_0 C^{1/2}/G^2. \tag{11}$$

For a wavelength $\lambda > \lambda_{\max}$, no three-beam diffraction is possible. When $\lambda = \lambda_{\max}$, the three-beam case is planar as employed for beam splitting in the interferometer by Graeff & Bonse (1977). For $\lambda < \lambda_{\max}$, we have non-planar three-beam cases which solely are of interest here. It is obvious from Fig. 3 that, for the beam widening to function, a wavelength λ considerably smaller than $\lambda_{\max}$ has to be used.

Of importance is also the unit normal $\mathbf{n}_\perp = (n_{\perp 1}, n_{\perp 2}, 0)$ in the vertical direction for which we find

$$n_{\perp 1} = C^{-1}(hF\cos\Theta_B + kG\sin\Theta_B), \tag{12}$$

$$n_{\perp 2} = C^{-1}(kF\cos\Theta_B - hG\sin\Theta_B). \tag{13}$$

From equations (4)–(10) we find the unit vector $\mathbf{s}^+ = (s_1, s_2, s_3)$ in the direction of a diffracted wave

$$s_1 = C^{-1}(kF\cos\Theta_B - hG\sin\Theta_B) + \lambda h/a_0, \tag{14}$$

$$s_2 = C^{-1}(-hF\cos\Theta_B - kG\sin\Theta_B) + \lambda k/a_0, \tag{15}$$

$$s_3 = \lambda l/a_0. \tag{16}$$

Next we consider the ray which travels in the direction of the diffracted wave bridging the gap between wafers S and M1 of width y_1,

$$\mathbf{r}_{SM1} = \mathbf{s}^+ y_1/(\mathbf{s}^+\cdot\mathbf{n}_c). \tag{17}$$

Its projection in the vertical direction, $\mathbf{r}_{SM1}\cdot\mathbf{n}_\perp$, is the distance Δz between interfering beams. With equations (1)–(2), (9)–(10) and (12)–(17) we obtain

$$\Delta z = 2y_1 \sin\Theta_B\left(1 + l^2/C\right)^{-1/2}. \tag{18}$$

The amount W of horizontal separation of beams hkl, $hk\bar{l}$ is twice the projection of the ray of equation (17) along the horizontal [001]. We find

$$W = 2y_1 \sin\varepsilon\left(\cos^2\Theta_B - \sin^2\Theta_B l^2/C\right)^{-1/2}. \tag{19}$$

where $\sin\varepsilon = \{l\lambda/a_0\}$. 2ε is the angle between beams $\mathbf{K}_{hkl}$ and $\mathbf{K}_{hk\bar{l}}$.

Δz and W are important criteria for choosing three-beam reflections suitable for use with given sample dimensions, sample absorption properties and X-ray energy E. The latter is often determined mainly by sample absorption. Using the described algorithm, we surveyed a large number of reflections for energies ranging from 10 keV to 105 keV. In Table 1 we list some typical and possibly useful choices of reflections at 80 keV (20 keV) for an interferometer with $y_1 = 31.7$ mm ($y_1 = 27.8$ mm).

5. Conclusion and outlook

We have for the first time employed non-planar multiple-beam diffraction in an X-ray interferometer and were able to successfully apply it to X-ray interferometric PμCT. The pilot experiment presented proves that the phase-sensing abilities and the reconstruction process are not affected by multiple diffraction inside the optical components S, M1, M2 and A of the interferometer. We show that PμCT is well feasible up to photon energies of at least 71 keV. Furthermore, we have illustrated that multiple diffraction can very profitably be employed to widen narrow beams delivered by present synchrotron radiation sources and to adapt the beam geometry to growing sample dimensions. Multiple-beam diffraction can also be used in interferometry with thermal neutrons (Bauspiess *et al.*, 1974). Finally, we have presented a simple algorithm for surveying the properties of three-beam cases of the $h\ k\ \pm l$ type over a wide range of energies and include exemplary results useful for PμCT using synchrotron radiation.

We thank J. R. Schneider and T. Lippmann of DESY for fruitful discussions regarding the use of beamline BW5 of HASYLAB, and T. Biermann for manufacturing the interferometer and for help during the PμCT measurements. Financial support by the Minister for Wissenschaft und Forschung, NRW (Düsseldorf), is gratefully acknowledged.

References

Bauspiess, W., Bonse, U., Rauch, H. & Treimer, W. (1974). *Z. Phys.* **271**, 177–182.
Beckmann, F., Bonse, U., Busch, F., Günnewig, O. & Biermann, T. (1995). *HASYLAB Annual Rep. II*, pp. 691–692. HASYLAB, Hamburg, Germany.
Beckmann, F., Bonse, U., Busch, F., Günnewig, O. & Biermann, T. (1997). *J. Comput. Assist. Tomogr.* **21**, 539–553.
Bonse, U. & Hart, M. (1965*a*). *Appl. Phys. Lett.* **6**, 155–156.
Bonse, U. & Hart, M. (1965*b*). *Appl. Phys. Lett.* **7**, 99–100.
Bonse, U. & Busch, F. (1996). *Prog. Biophys. Molec. Biol.* **65**, 133–169.
Graeff, W. & Engelke, K. (1991). *Handbook of Synchrotron Radiation*, edited by S. Ebashi, M. Koch & E. Rubinstein, pp. 361–405. Amsterdam: Elsevier Science.

Graeff, W. (1996). *Proceedings of the International School of Physics Enrico Fermi*, Course CXXVII, edited by. E. Burattini & A. Balerna, pp. 155–170. Amsterdam: IOS Press.
Graeff, W. & Bonse, U. (1977). *Z. Phys. B*, **27**, 19–32.
Kak, A. C. & Slaney, M. (1987). *Principles of Computerized Tomographic Imaging*. New York: IEEE Press.
Kinney, J. H. & Nichols, M. C. (1992). *Annu. Rev. Mater. Sci.* **22**, 121–152.
Momose, A., Takeda, T. & Y. Itai, Y. (1995). *Rev. Sci. Instrum.* **66**(2), 1434–1436.

 Received 7 September 2000 • Accepted 2 November 2000